POLITECNICO DI TORINO
Repository ISTITUZIONALE

Theoretical investigation of BeZnO-based UV LEDs

(Article begins on next page)

02 April 2023

Theoretical Investigation of BeZnO-Based UV LEDs

R. Ganmukhi†, M. Calciati‡, M. Goano‡♯, and E. Bellotti†§

† ECE Department, Boston University, 8 Saint Mary's Street, 02215 Boston, MA

‡ Dipartimento di Elettronica e Telecomunicazioni, Politecnico di Torino, corso Duca degli Abruzzi 24, I-10129 Torino, Italy

♯ IEIIT-CNR, Politecnico di Torino, corso Duca degli Abruzzi 24, 10129 Torino, Italy

Abstract. Two-dimensional numerical simulation is employed to assess a number of possible design approaches aimed at optimizing the internal quantum efficiency of BeZnO-based light-emitting diodes grown along the c-axis. First, we describe the material parameters and the numerical simulation methods used to study these devices. Second, the effects of thickness, doping, and alloy composition of the BeZnO electron blocking layer are analysed in order to maximise the carrier confinement in the active region. The optimum number of quantum wells and barrier doping level are also addressed, as well as the effects of the buffer layer thickness. Finally, the limitations on the device performance imposed by the nonuniform lateral current distribution are discussed.

§ Corresponding author: `bellotti@bu.edu`

1. Introduction

Light-emitting diodes (LEDs) intended to operate in the ultraviolet (UV) spectral range are of great interest for a number of applications [1]. In addition to sharing the attractive features common to all LEDs (low power consumption, relatively low manufacturing costs, flexibility in tailoring the emission spectrum, fast switching time), UV LEDs would be an ideal alternative to mercury-based lamps in water purification applications and could have several biological applications such as bioagent detection and surface decontamination.

One material system with the potential of leading to efficient UV LEDs is zinc oxide (ZnO) and its ternary compounds (MgZnO and BeZnO). ZnO is a direct band-gap II-VI compound semiconductor with energy gap $E_g \approx 3.4\,\text{eV}$. Due to defects in the material, as-grown ZnO is normally unintentionally n-type, while p-type doping techniques still face significant challenges.

In order to design active regions for LEDs, a barrier material with energy gap larger than ZnO is needed, and both MgZnO and BeZnO are possible choices. Although MgZnO is technologically more mature, BeZnO may potentially offer some advantages. In fact, since BeO and ZnO share the same hexagonal symmetry, phase segregation in BeZnO is a far less critical issue than in MgZnO and, in principle, the energy band gap of BeZnO can be engineered to range from $3.4\,\text{eV}$ (ZnO) to $10.6\,\text{eV}$ (BeO) by changing the Be molar fraction. This makes it possible to grow barrier layers with higher confinement than what can be obtained with MgZnO, potentially leading to better performance in the deep-UV spectral range. Ryu and coworkers [2, 3] have shown that it is indeed possible to grow BeZnO-based LED and laser structures. Therefore, it is important to provide the ZnO community with a preliminary evaluation of the BeZnO potential as a LED material.

The manuscript is organized as follows. Section 2 provides a complete set of models for the material parameters involved in the numerical simulation of BeZnO-based LEDs. Section 3 presents a systematic comparison of different ZnO/BeZnO LED structures, with the aim of determining the structural and doping parameters corresponding to the maximum internal quantum efficiency (IQE). Finally, section 4 concludes the study detailing the most significant outcomes.

2. Numerical simulation model

Our device analysis is based on the APSYS modelling software from Crosslight Software [13,14]. This software implements a two-dimensional coupled drift-diffusion/Schrödinger model. A realistic description of BeZnO-based LEDs requires a significant amount of information about the material parameters. Table 1 collects the most important structural and electronic properties of $\text{Be}_x\text{Zn}_{1-x}\text{O}$ as functions of the Be molar fraction x: lattice constants a, c, energy gap E_g, spin-orbit and crystal-field splitting Δ_so, Δ_cr, static relative dielectric constant ε_0, transverse and longitudinal components of the electron

Table 1. Material parameters used for $\text{Be}_x\text{Zn}_{1-x}\text{O}$ $(0 \leq x \leq 1.0)$ at $T = 300\,\text{K}$

a, Å	$3.25 - 0.533x$ [4]
c, Å	5.2058 [5]
E_g, eV	$3.373 + 3.287x + 3.925x^2$ [6]
Δ_{so}, meV	$13.59 + 11.3x$ [7]
Δ_{cr}, meV	$38 + 8.35x$ [7]
ε_0	$8.1 - 5.2x$ [8]
$m_e^{\parallel}$	$0.23 + 0.35x$ [9]
$m_e^{\perp}$	$0.21 + 0.52x$ [9]
A_1	$-3.78 + 1.27x$ [10]
A_2	$-0.44 - 0.02x$ [10]
A_3	$3.45 - 1.24x$ [10]
A_4	$-1.63 + 0.91x$ [10]
A_5	$-1.68 + 0.78x$ [10]
A_6	$-2.23 + 1.2015x$ [10]
D_1, eV	-3.9 [11]
D_2, eV	-4.13 [11]
D_3, eV	-1.15 [11]
D_4, eV	1.22 [11]
D_5, eV	1.53 [11]
D_6, eV	2.83 [11]
c_{11}, GPa	$209 + 223.5x$ [6]
c_{12}, GPa	$120 + 15.8x$ [6]
c_{13}, GPa	$104 - 5x$ [6]
c_{33}, GPa	$216 + 258.1x$ [6]
c_{44}, GPa	$44 + 87.3x$ [6]
e_{13}, $\text{C}\,\text{m}^{-2}$	$-0.53 + 0.46x$ [12]
e_{33}, $\text{C}\,\text{m}^{-2}$	$1.19 - 1.15x$ [12]
P_{sp}, $\text{C}\,\text{m}^{-2}$	$-0.057 + 0.021x$ [12]

Table 2. Carrier transport and recombination parameters used for BeZnO

A, s^{-1}	$2{\cdot}10^{10}$
B, $\text{cm}^3\,\text{s}^{-1}$	$2{\cdot}10^{-11}$
C, $\text{cm}^6\,\text{s}^{-1}$	10^{-34}
μ_{min_e}, $\text{cm}^2\,\text{V}^{-1}\text{s}^{-1}$	50
μ_{max_e}, $\text{cm}^2\,\text{V}^{-1}\text{s}^{-1}$	300
N_{0e}, cm^{-3}	10^{18}
α_e	1
μ_{min_h}, $\text{cm}^2\,\text{V}^{-1}\text{s}^{-1}$	1
μ_{max_h}, $\text{cm}^2\,\text{V}^{-1}\text{s}^{-1}$	20
N_{0h}, cm^{-3}	10^{17}
α_h	1

effective mass $m_e^\perp$, $m_e^\parallel$, Luttinger parameters $A_1, \ldots A_6$ of the **k·p** Hamiltonian, valence band deformation potentials $D_1, \ldots D_6$, and spontaneous polarization P_{sp}. Although a large number of experimental and theoretical studies have been performed on the ZnO and BeO electronic structure, there is still a significant uncertainty about the values of several details for BeO and BeZnO. In this work we employ the description of the electronic structure adopted in [14], derived from an extensive analysis of the available theoretical and experimental data [5, 11, 15–20]. A quadratic approximation has been adopted for the energy gap $E_g(x) = xE_g(\mathrm{BeO}) + (1-x)E_g(\mathrm{ZnO}) - b\,x\,(1-x)$ with a positive bowing factor b. For all other parameters we have assumed a linear dependence from x, with a few exceptions where the ZnO value has been used over the entire alloy composition range. The heterobarriers in the active regions have been modeled assuming a conduction band offset ΔE_c equal to 65% of the energy gap difference between ZnO and BeZnO of a given composition (see also [21]).

An important issue in the design of BeZnO-based LEDs is the determination of realistic estimates for the spontaneous and piezoelectric charges. In all semiconductor materials with wurtzite crystal structure, the uniaxial nature of the crystal leads to the presence of a spontaneous polarization, which is accompanied by a piezoelectric component when the material is under mechanical stress. This effect has to be properly accounted for when dealing with multiple quantum well (MQW) LEDs and lasers because the internal electric fields due to the polarization charges lead to quantum-confined Stark effect, which affects the emission wavelength and reduces the oscillator strength causing a drop in IQE. To account for piezoelectric polarization we include piezoelectric charges at the interfaces as:

$$P_{\mathrm{pz}} = 2\frac{a_s - a}{a}\left(e_{31} - e_{33}\frac{c_{13}}{c_{33}}\right) \tag{1}$$

where e_{ij} and c_{ij} are the elastic and piezoelectric constants and a_s and a are the strained and relaxed lattice constants. As in the case of III-nitrides [22], we assume that the orientation of the spontaneous and piezoelectric polarization is defined with a positive direction that goes from the metal (cation) to the oxygen atom (anion) along the c-axis. From Table 1 one can see that spontaneous polarization is negative for the whole composition range of BeZnO. As a result, spontaneous polarization is directed towards the substrate for Zn-face grown material and towards the top surface for O-face grown material, as shown in figure 1. Furthermore, since $(e_{31} - e_{33}c_{13}/c_{33}) < 0$ for BeZnO, P_{pz} is negative for tensile strain and positive for compressive strain. A ZnO QW grown on a BeZnO buffer layer is under compressive strain and P_{pz} is antiparallel to P_{sp}. In case the stack is grown on the Zn face, P_{sp} is directed towards the substrate while P_{pz} is directed toward to top of the device (see figure 1(a)). The opposite is valid for an O-face substrate (figure 1(b)). In a heterostructure grown on the Zn face and composed of a top and a bottom layer, the total polarization P_{tot} is:

$$P_{\mathrm{tot}} = P_{\mathrm{bottom}} - P_{\mathrm{top}} = (P_{\mathrm{sp,bottom}} + P_{\mathrm{pz,bottom}}) - (P_{\mathrm{sp,top}} + P_{\mathrm{pz,top}}) \tag{2}$$
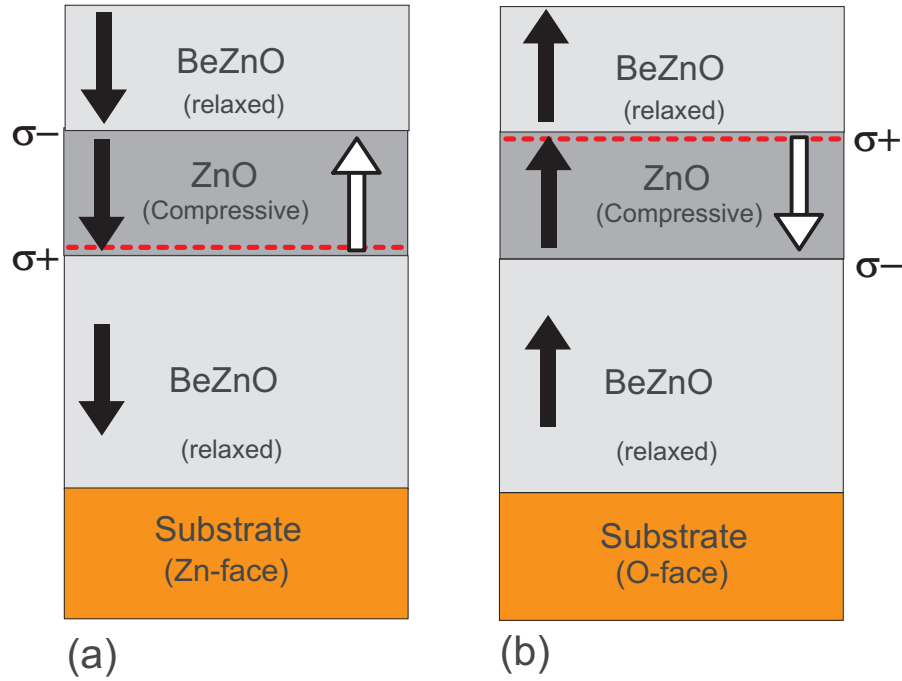
Figure 1. Configuration of the spontaneous and piezoelectric polarization (white and black arrows, respectively) for $Be_xZn_{1-x}O/ZnO/Be_xZn_{1-x}O$ stacks grown on both Zn-face and O-face substrates.

while, for a heterostructure grown on the O face, it becomes:

$$P_{tot} = P_{top} - P_{bottom} = (P_{sp,top} + P_{pz,top}) - (P_{sp,bottom} + P_{pz,bottom}) \qquad (3)$$

In the case of a ZnO/BeZnO interface, assuming that the Zn-face grown BeZnO layer is completely relaxed and, as a consequence, its piezoelectric contribution is negligible, there will be positive interface charges and a resulting accumulation of electrons at the bottom ZnO/BeZnO interface, as shown in figure 1(a). If the structure is grown on the O face, the electron accumulation occurs at the top ZnO/BeZnO interface, as shown in figure 1(b).

Table 2 provides the transport and recombination parameters employed to model carrier transport in the LED structure. Due to the paucity of experimental data available on BeZnO, the ZnO parameters of the low-field mobility models for electrons and holes [23–25], fitted from the results of Monte Carlo transport simulations [26], have been used for any alloy composition, while the Auger recombination coefficient has been derived by recent *ab initio* results on ZnO and MgZnO [27].

3. Results

In this section we address the design tradeoffs and determine the optimal structure parameters for BeZnO-based LEDs. First we examine the effect of the choice of molar fraction, doping and thickness of the electron blocking layer (EBL). Subsequently we discuss the optimum number of QWs and the impact of barrier doping and buffer
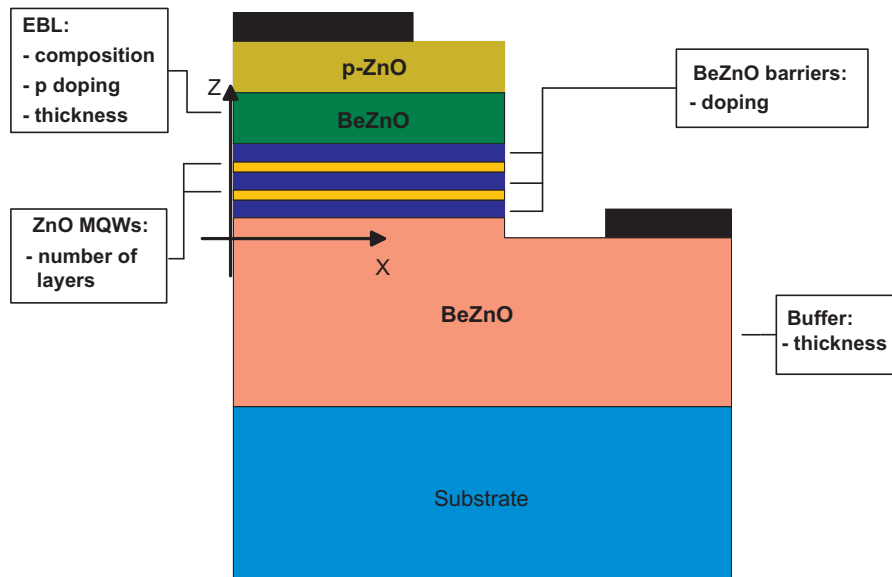
Figure 2. Schematic cross section of the considered BeZnO-based LED structure, outlining the regions whose parameters have been changed in order to optimize the IQE. The x and z axes are used as references for the figures presenting the band profiles and carrier distributions.

Table 3. Thickness, doping level and composition of the reference BeZnO-based LED structure considered in the present work

Layer	Thickness, nm	Doping, cm^{-3}	Composition	E_g
p-cap	550	$5 \cdot 10^{18}$	ZnO	3.373 eV
p-cladding	10	$5 \cdot 10^{18}$	Be$_{0.06}$Zn$_{0.94}$O	3.62 eV
EBL	10	$5 \cdot 10^{18}$	Be$_{0.12}$Zn$_{0.88}$O	3.80 eV
well	2.2	undoped	ZnO	3.37 eV
barrier	8	undoped	Be$_{0.07}$Zn$_{0.93}$O	3.62 eV
buffer	2500	$5 \cdot 10^{18}$	Be$_{0.12}$Zn$_{0.88}$O	3.80 eV

layer thickness. Finally, we address the critical effects of lateral nonuniformities in the distribution of current and radiative recombination.

To evaluate the BeZnO-based LED performance, we start from the reference structure presented in figure 2. The LED is grown on a sapphire substrate designed for a 360 nm emission wavelength. On top of the substrate is a relaxed BeZnO 3.0 μm thick buffer layer with n-doping of $5 \cdot 10^{18}$ cm^{-3} and 11.5% Be molar fraction. This is effectively a window layer from which light is extracted out of the back-side of the device. This layer is followed by the BeZnO/ZnO active region containing three ZnO QWs separated by Be$_{0.07}$Zn$_{0.93}$O barriers. On top of the active region is a 10 nm thick p-doped ($5 \cdot 10^{18}$ cm^{-3}) Be$_{0.115}$Zn$_{0.885}$O EBL. The EBL is followed by a 10 nm thick Be$_{0.05}$Zn$_{0.95}$O cladding layer with p-doping of $5 \cdot 10^{18}$ cm^{-3}. Finally the device is capped by a 550 nm thick ZnO layer with p-doping $5 \cdot 10^{18}$ cm^{-3}. The widths of substrate and mesa are 300 μm and 200 μm, respectively, while the metallic contact deposited on the p-ZnO cap has a width $W_c = 75\,\mu$m. All band diagrams and carrier density profiles along
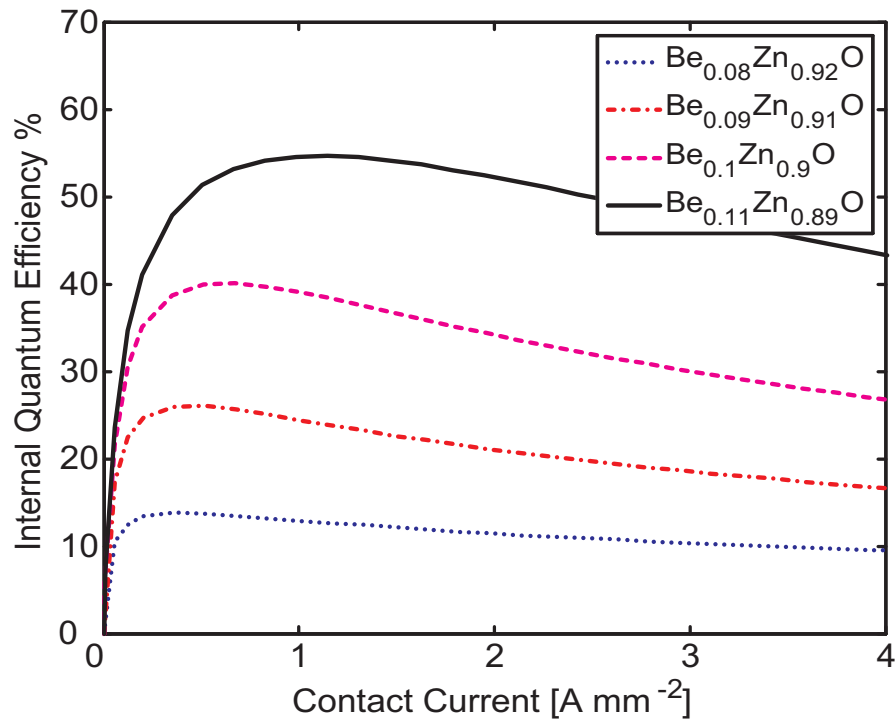
Figure 3. Calculated IQE as a function of the current density for a Be molar fraction in the EBL equal to 8%, 9%, 10%, 11%.

the z coordinate reported in the following sections have been calculated at a distance $x = 50\,\mu$m from the left sidewall of the mesa.

3.1. EBL design parameters

An optimal selection of the Be molar fraction in the $\mathrm{Be}_x\mathrm{Zn}_{1-x}\mathrm{O}$ EBL is critical for maximizing the IQE. In fact, as x is increased, the EBL forms a larger energy barrier to block the electrons from leaking into the cap layer from the active region. Figure 3 presents the calculated IQE as a function of current density for a number of EBL alloy compositions. As x is increased from 0.08 to 0.11, the IQE is drastically increased; further x increases do not improve the IQE, since the valence band discontinuity reduces the hole injection from the p-type region. To understand the effect of the EBL we examine both the profiles of conduction and valence bands and the carrier concentrations as a function of EBL molar fraction at a given current density. Figure 4 presents the calculated energy band diagrams across the active region for a Be molar fraction in the EBL equal to 8% (green), 9% (black), 10% (red), 11% (blue) at a current density $2.3\,\mathrm{A/mm^2}$. We can observe that the energy barrier seen from the rightmost well, at $z \approx 0.05\,\mu$m, increases to about $0.6\,\mathrm{eV}$ when x is changed from 0.08 to 0.11. At the same time the barrier seen by holes increases only of about $50\,\mathrm{meV}$. This leads to a significant reduction in electron leakage with a minor reduction of the hole injection efficiency, and consequently a drastic improvement in the IQE. Further confirmation of the confining role of the EBL comes from the analysis of the carrier concentrations that are presented
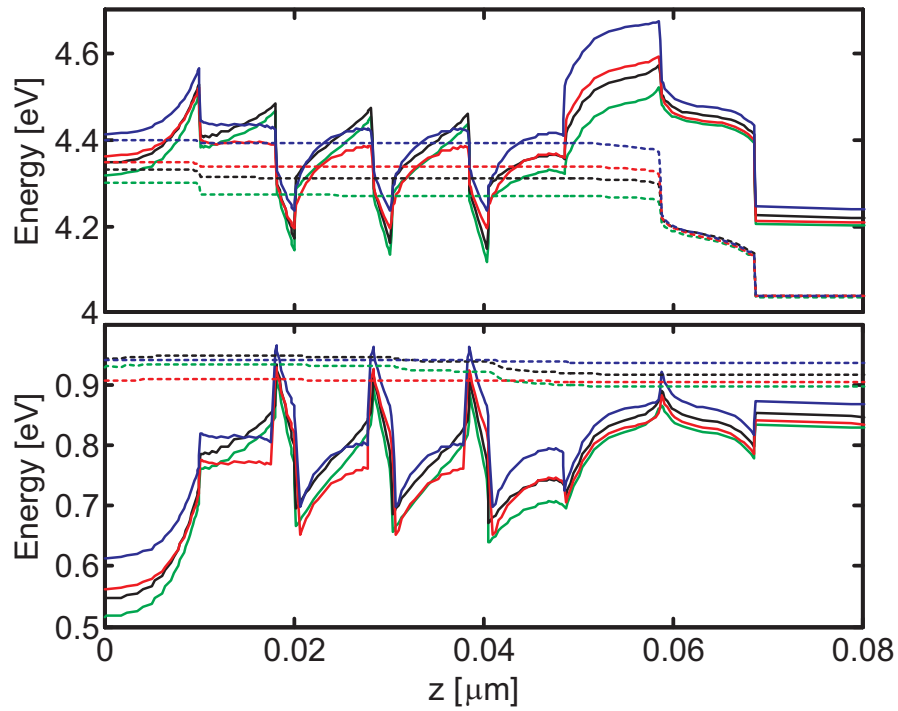
Figure 4. Calculated energy band diagrams across the active region of a structure grown on the metal face, for the Be molar fractions in the EBL equal to 8% (green), 9% (black), 10% (red), 11% (blue) as considered in figure 3 at a current density $2.3\,\text{A/mm}^2$. The quasi-Fermi levels of electrons and holes are reported (dashed lines) along with the conduction band (top) and the valence band (bottom).
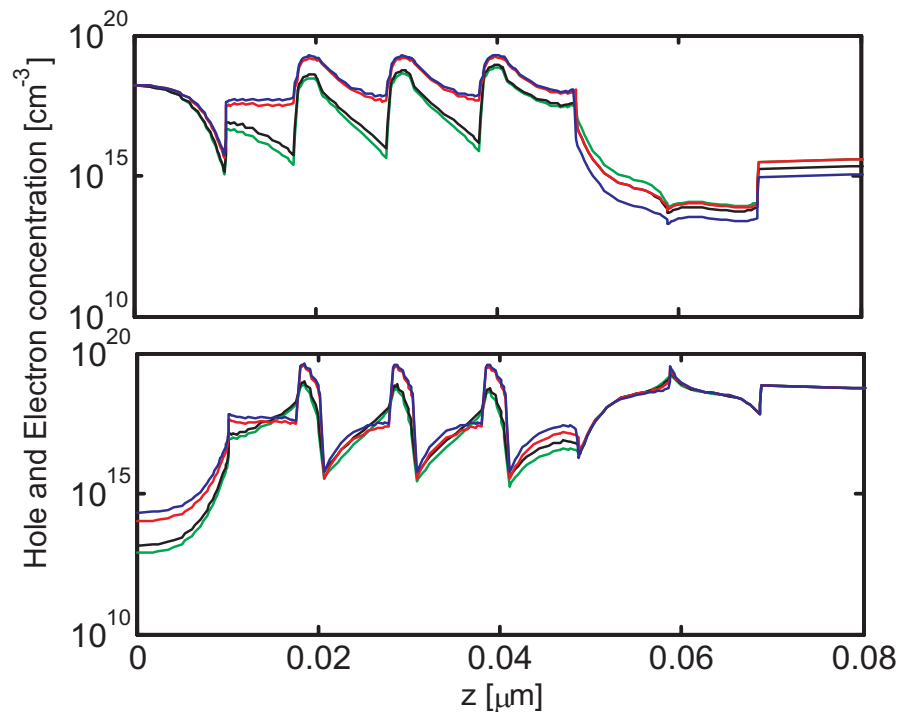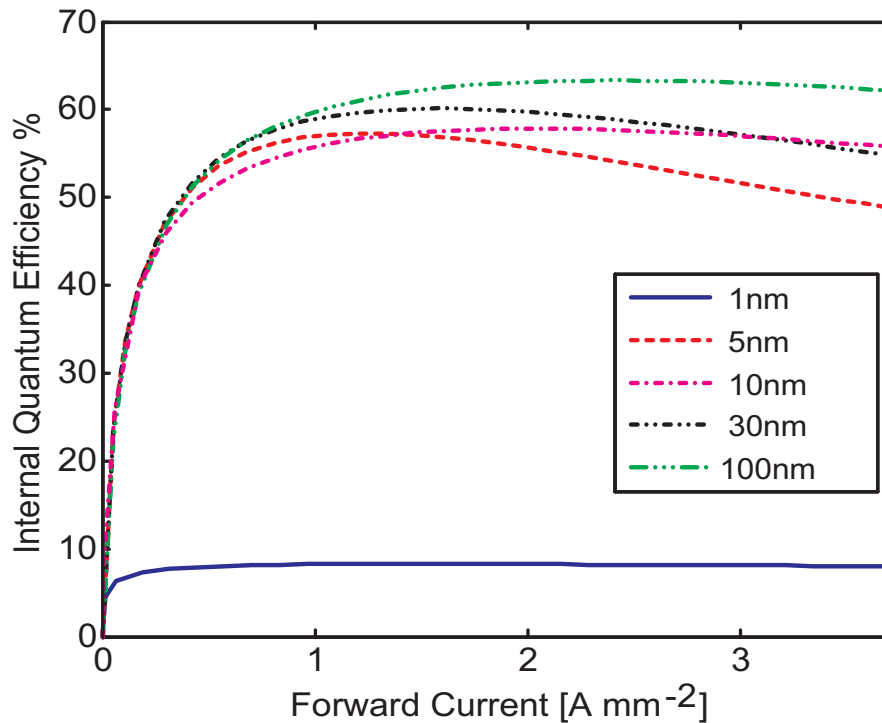

Figure 5. Calculated electron (top) and hole (bottom) density across the active region for the Be molar fractions in the EBL equal to 8% (green), 9% (black), 10% (red), 11% (blue) as considered in figure 3 at a current density $2.3\,\text{A/mm}^2$.

Figure 6. Calculated IQE as a function of the current density for different EBL thicknesses.

in figure 5. It can be seen that a $Be_{0.11}Zn_{0.89}O$ EBL leads to an electron concentration in the active region that is between one and two orders of magnitude larger than in the case of a $Be_{0.08}Zn_{0.92}O$ EBL, while the hole concentration is only slightly reduced.

The results presented in figure 3, 4 and 5 assume that the thickness of the EBL is 5 nm. Figure 6 presents the calculated IQE as a function of current for an EBL with $x = 0.11$ and several layer thicknesses. We can immediately notice that for thicker EBLs not only the IQE increases but the reduction of IQE at higher injection currents is less pronounced. This is clearly due to the fact that for a given Be molar fraction, there is a minimum layer thickness necessary to block the electron leakage into the cap region. In the case of a $Be_{0.11}Zn_{0.89}O$ EBL, a thickness between 50 nm and 100 nm leads to an IQE above 60%.

The last design parameter to consider for the EBL is its doping. In the calculations performed so far we have assumed that the EBL is p-doped with $5 \cdot 10^{18}$ cm^{-3} acceptors. This level of carrier concentration in $Be_{0.11}Zn_{0.89}O$ is clearly out of reach when one considers the current state of the art of the ZnO material system development. The calculated IQE as a function of current density for several different EBL p-type doping levels is presented in figure 9. It can be seen that p-type doping of the EBL is critical to boost the IQE. This conclusion was also reached for ZnO/MgZnO [14] and GaN/AlGaN [28] based devices. As the EBL doping level is increased from undoped to $5 \cdot 10^{19}$ cm^{-3}, the IQE increases significantly. The reason why increasing the doping level is effective in improving the IQE can be traced back to the hole injection process
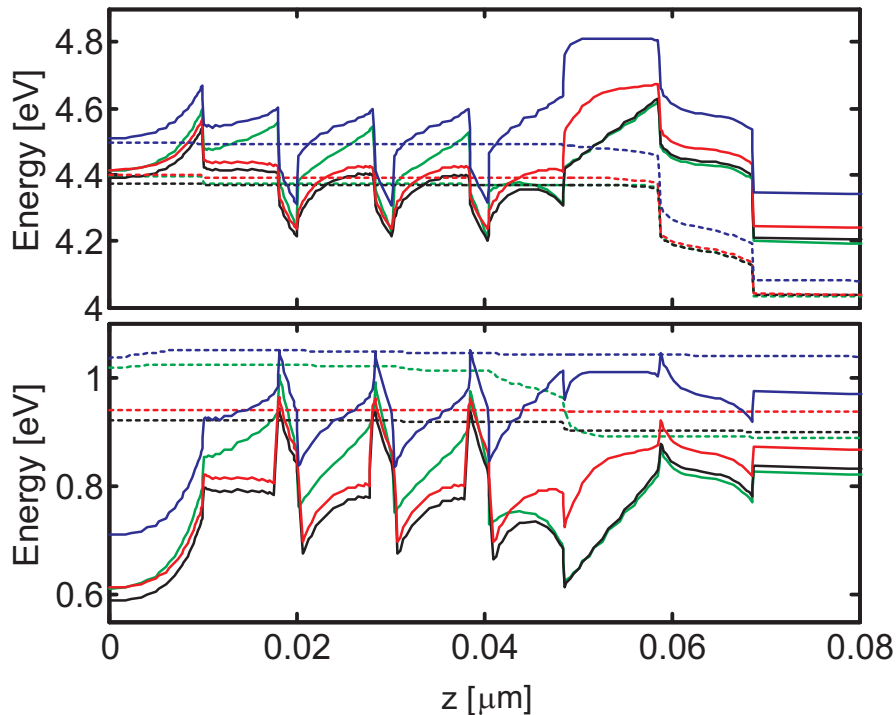
Figure 7. Calculated energy band diagrams across the active region, for an EBL
p-type doping level equal to zero (green), $5 \cdot 10^{16}$ cm^{-3} (black), $5 \cdot 10^{18}$ cm^{-3} (red),
$5 \cdot 10^{19}$ cm^{-3} (blue). The quasi-Fermi levels of electrons and holes are reported (dashed
lines) along with the conduction band (top) and the valence band (bottom) at a current
density 2.3 A/mm^2.

in the active region. This can be observed in figure 7, that presents the calculated
energy band diagrams across the active region for an EBL *p*-type doping level equal to
zero (green), $5 \cdot 10^{16}$ cm^{-3} (black), $5 \cdot 10^{18}$ cm^{-3} (red), $5 \cdot 10^{19}$ cm^{-3} (blue) at a current
density 2.3 A/mm^2. For a given EBL composition, an adequate EBL *p*-doping will lower
the valence band barrier for hole injection from the *p*-type cap while at the same time
increasing the barrier from electron escape from the active region. This can be observed
in figure 7 looking at the blue line that represents the valence band profile for an EBL
doping of $5 \cdot 10^{19}$ cm^{-3}. In this case there is a small barrier for holes moving from the
p-type cap to the active region. Figure 8 further underscores this phenomenon. In fact,
the increased doping in the EBL and the resulting reduction of barrier for holes, lead
to a hole concentration that is several order of magnitude larger than in the case of an
undoped EBL.

From the simulation results presented up to this point, it is clear that the most
critical parameter for optimizing the LED performance is the EBL doping. In fact,
while the EBL thickness and composition can be relatively well controlled and they are
technologically feasible, the high doping concentration and acceptor activation required,
of the order of 10^{18} cm^{-3}, is not currently technologically feasible. This clearly leads to
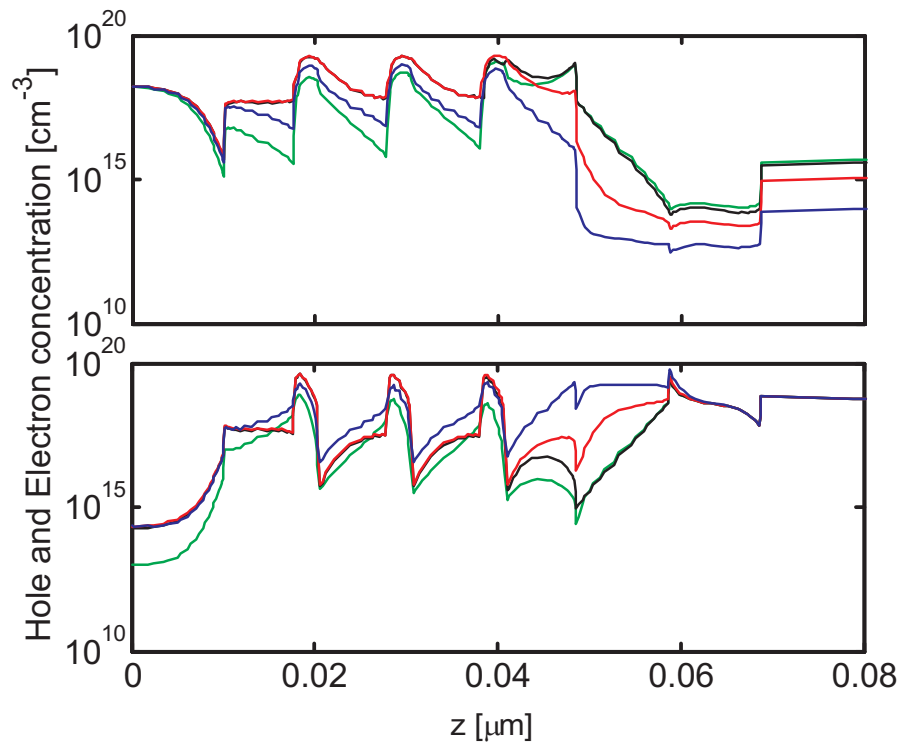a severe limitation on the IQE that can be reached.

Figure 8. Calculated electron (top) and hole (bottom) density across the active region for the EBL p-type doping level equal to zero (green), $5 \cdot 10^{16}$ cm^{-3} (black), $5 \cdot 10^{18}$ cm^{-3} (red), $5 \cdot 10^{19}$ cm^{-3} (blue) as considered in figure 7.
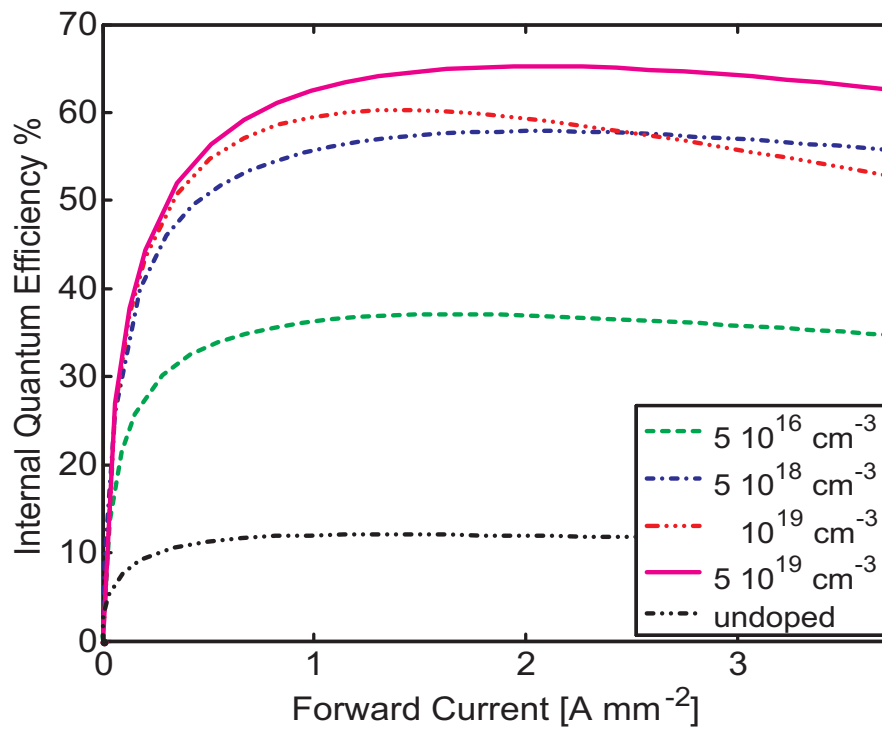

Figure 9. Calculated IQE as a function of the current density for the EBL doping levels considered in figure 7.
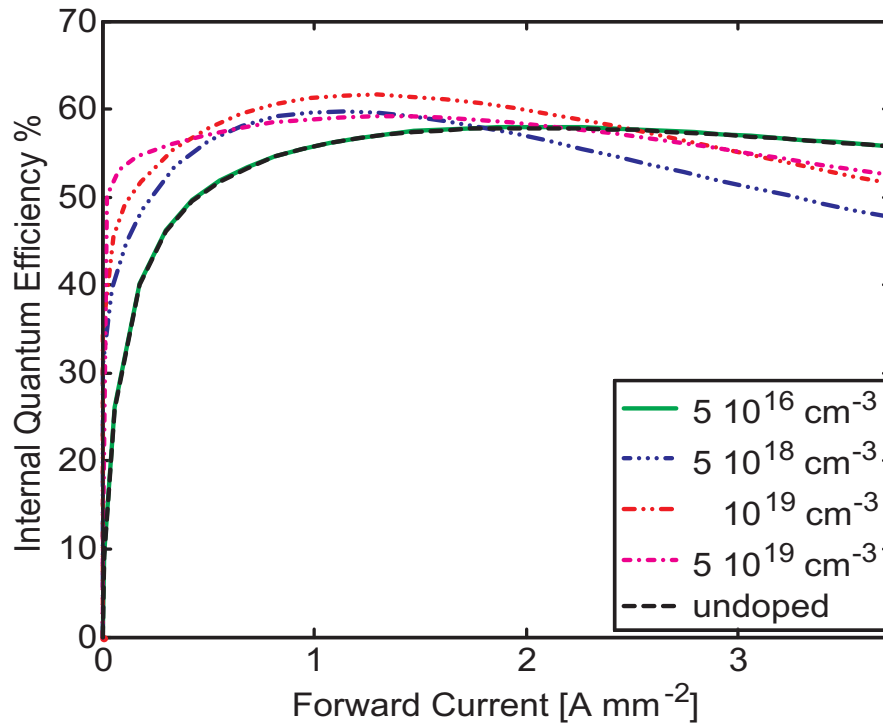
Figure 10. Calculated IQE as a function of the current density for several barrier doping levels.

3.2. Barrier doping

Several groups [29–31] have proposed to use *p*-type doping in the QW barriers to compensate for the presence of interface charges and effectively increase the IQE. Figure 10 presents the calculated IQE data as a function of the current density for different barrier *p*-type doping levels. As seen by the results, even with undoped barrier the IQE is above 50%, and an increase by several order of magnitude of the barrier doping leads to a marginal increase in the IQE. This shows once again that an effective EBL doping is key to obtain a significant improvement in IQE. Furthermore, the barrier doping needed to overcome the internal polarization field is fairly high, above 10^{19} cm^{-3}, which makes this approach practically impossible for BeZnO-based devices.

3.3. Number of quantum wells

Another important design issue related to the device active region is the selection of the optimum number of quantum wells (QWs). Several studies have pointed out that, because of the limited hole mobility, a large number of QWs may lead to a situation where, at a given injection level, the QWs that are located farther away from the cap layer are scarcely populated with holes and are inactive from the point of view of optical generation. Clearly, the optimum number of QWs depends on several factors, including well width and capture/escape rates. Holes, with a much lower mobility than electrons, tend to fill the wells closer to the *p*-contact, while electrons are free to diffuse to more
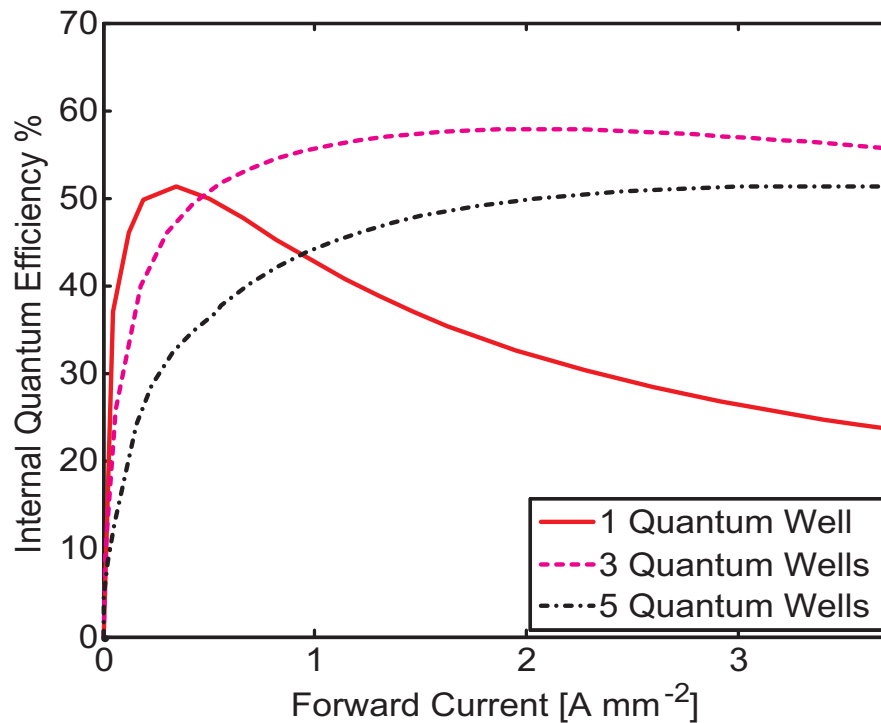
Figure 11. Calculated IQE as a function of the current density for a number of QWs in the active region ranging from 1 to 5.

distant wells. Narrow wells allow a reduction on the effects of interface charges, but too narrow wells can lead to larger carrier fly-over. Figure 11 presents the IQE as a function of current density for a variable number of QWs. As illustrated by this figure, a device with a single QW may be the best choice for operation at low injection levels, but at more practical current level densities, up to $3\,\mathrm{A/mm^2}$, three QWs is the optimal choice. We also notice that, to fully exploit a five-QW device, much higher current densities have to be used.

3.4. Buffer layer thickness

The last design parameter we consider is the thickness of the buffer layer. This has a significant effect on the current-voltage characteristics as well as on the wall-plug efficiency of the device. In fact, in the case of a device where the light is extracted from the back side (substrate), the buffer layer introduces lateral access regions that have a finite resistance. Varying the buffer layer thickness will vary the effective internal resistance of the device and therefore the efficiency. Figure 12 presents the calculated total emitted optical power, integrated over the entire device volume, assuming an extraction efficiency of 0.5, as a function of the applied bias for different buffer layer thicknesses ranging from 0.5 to $3.0\,\mu$m and constant n-doping of $5{\cdot}10^{18}\,\mathrm{cm^{-3}}$. The inset of the same figure shows the voltage-current characteristics of the device for the same buffer layer thickness values.
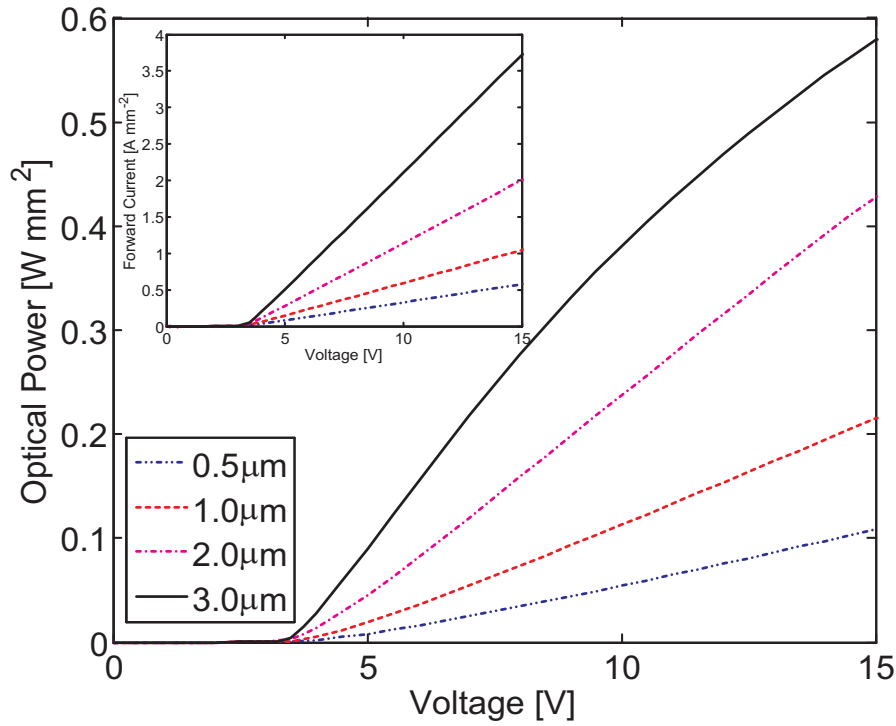
Figure 12. Calculated emitted optical power and corresponding current density as functions of the applied voltage for several buffer layer thicknesses.

It can be seen that, if one considers an operating voltage in the 5 V to 10 V range, a thicker buffer layer will lead to a higher output power. In fact, since thinner layers have higher series resistances, for a given voltage the resulting current density is lower. On the other hand, if one keeps the current density fixed, for example at $2\,\mathrm{A/mm^2}$, the device with the thicker buffer layer ($3\,\mu$m) will require a voltage of $\approx 8\,$V while for a $2\,\mu$m-thick buffer layer a 15 V bias is needed. It is clear from these results that a thick buffer layer is needed to overcome the limitations due to the poor n-type mobility in these alloys.

3.5. Lateral distribution of current and radiative recombination

An issue which is often neglected in LED design and optimization is the influence on device performance of the nonuniformity along the lateral direction of the current and radiative recombination distributions. Most lateral LED structures suffer from significant current crowding effects, namely the tendency of majority carriers to flow in a limited section of the device, thus leading to higher than normal ohmic losses and inefficient use of the device bulk. This effect arises from the fact that the lateral metallic contact on the n-type buffer layer imposes a nonuniform bias on the active region, and could be mitigated using a vertical device configuration [32, 33], where the n-side contact is placed on the substrate beneath the active region. Current crowding can be also influenced by the geometry of the p-side contact, and in this section we

analyze current crowding in the device under study by considering the effects of two different p-contact sizes. The results presented in the previous sections have been obtained assuming that the metallic contact deposited on the p-ZnO cap has a width $W_c = 75\,\mu$m. This contact covers only a small fraction of the entire mesa (see figure 2). To evaluate the current crowding effect we compare the current density distribution and the radiative emission in the active region of the device for two different dimensions of the p-contact, $W_c = 75\,\mu$m and $W_c = 200\,\mu$m, where the latter value corresponds to a contact covering completely the device mesa. Figure 13 presents the calculated dominant component $J_x(x)$ of the current density flowing through the active region for $W_c = 75\,\mu$m (Hc) and $W_c = 200\,\mu$m (Fc), respectively. The peak of the current density profile is located at a lateral coordinate corresponding to the edge of the metallic contact, near the center of the mesa for $W_c = 75\,\mu$m (dashed lines) and at the mesa sidewall for $W_c = 200\,\mu$m (solid lines). Current crowding also leads to severe nonuniformity in the light emission profile. Figure 14 presents the calculated lateral distribution of radiative recombination in the active region, which again has a peak in correspondence of the edge of the metallic contact. No significant efficiency improvement is observed when the p contact is extended to cover the entire mesa surface ($W_c = 200\,\mu$m) and the resulting radiative emission profile is confined to the outer edge of the mesa. In fact, the IQE is practically the same for both values of W_c, since the doubling of the peak value of radiative recombination for $W_c = 200\,\mu$m is offset by the halving of the region where radiative recombination is not negligible.

4. Conclusion

This paper has presented a preliminary theoretical study of the design criteria for BeZnO-based LED devices. Using a two-dimensional numerical model, we have investigated the possible design choices of the geometrical and electrical parameters of a reference LED structure intended to operate at a wavelength of 360 nm. We have evaluated the IQE as a function of the layer thicknesses and doping concentrations. Specifically, we have considered the dimension and doping of the EBL, the doping of the barriers and number of QWs in the active region, and the characteristics of the buffer layer. It has been found that, in the case of ZnO/BeZnO well/barrier active region, the most critical design parameter is the EBL doping. In fact, if the EBL is thicker than 10 nm and has a Be molar fraction in excess of 11%, it can operate effectively as long as the doping is p-type and at least equal to $5 \cdot 10^{18}\,\text{cm}^{-3}$. This is clearly outside the present range of practical feasibility for BeZnO. It has also been found that doping the barriers in the MQW region does not produce an appreciable improvement in the IQE. We have found that the optimum number of QWs in the active region is three for current densities between $1\,\text{A/mm}^2$ and $2\,\text{A/mm}^2$, while for higher current densities five QWs should be employed. We have also examined the effects of different buffer layer designs. Because of the low electron mobility of BeZnO alloys, we have concluded that a buffer layer with thickness larger than $2\,\mu$m is needed to operate the LED at voltages below
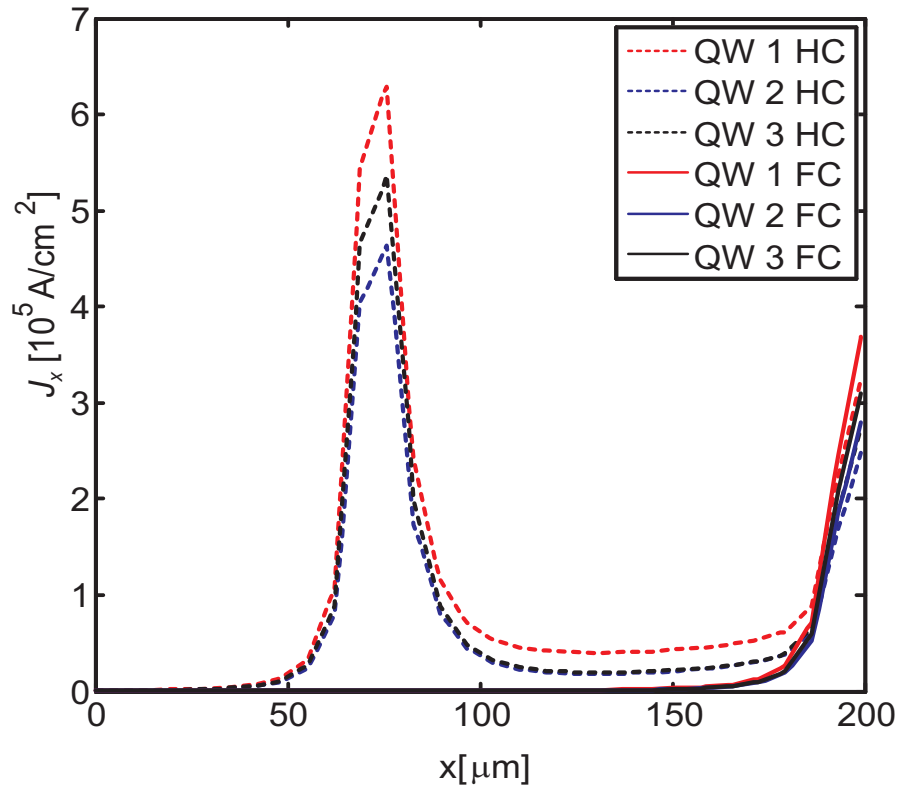
Figure 13. Calculated x-component of the current flowing through the active region for $W_c = 75\,\mu\text{m}$ (Hc) and $W_c = 200\,\mu\text{m}$ (Fc).

10 V and with IQE above 40%.

In conclusion, although BeZnO offers potential advantages for the design and fabrication of UV LEDs, it is still a relatively immature material. In order to be effectively used for LED design, significant developments in doping techniques and improvement in carrier mobility have to be achieved.
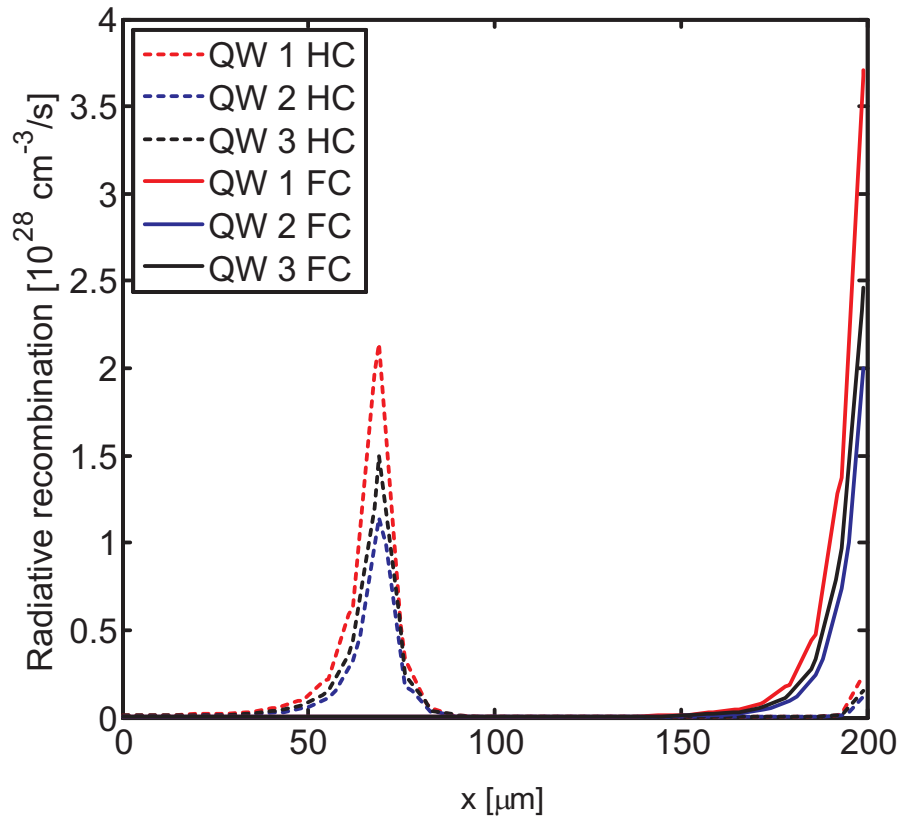
Acknowledgments

Figure 14. Calculated radiative recombination in the active region for $W_c = 75\,\mu$m (Hc) and $W_c = 200\,\mu$m (Fc).

References

[1] Shur M S and Gaska R 2010 Deep-ultraviolet light-emitting diodes *IEEE Trans. Electron Devices* **57**(1) 12–25

[2] Ryu Y R, Lee T S, Lubguban J A, Corman A B, White H W, Leem J H, Han M S, Park Y S, Youn C J and Kim W J 2006 Wide-band gap oxide alloy: BeZnO *Appl. Phys. Lett.* **88** 052103

[3] Kim W J, Leem J H, Han M S, Park I W, Ryu Y R and Lee T S 2006 Crystalline properties of wide band gap BeZnO films *J. Appl. Phys.* **99** 096104

[4] Madelung O 2004 *Semiconductors: Data Handbook* 3rd ed (Berlin: Springer-Verlag)

[5] Lambrecht W, Rodina A V, Limpijumnong S, Segall B and Meyer B K 2002 Valence-band ordering and magneto-optic exciton fine structure in ZnO *Phys. Rev. B* **65**(7) 075207

[6] Duan Y, Shi H and Qin L 2008 Elasticity, band structure, and piezoelectricity of $Be_xZn_{1-x}O$ alloys *Phys. Lett. A* **372** 2930–2933

[7] Xu Q, Zhang X W, Fan W J, Li S S and Xia J B 2008 Electronic structures of wurtzite ZnO, BeO, MgO and *p*-type doping in $Zn_{1-x}Y_xO$ (Y=Mg, Be) *Comp. Mater. Sci.* **44** 72–78

[8] Groh D, Pandey R, Sahariah M B, Amzallag E, Baraille I and Rérat M 2009 First-principles study of the optical properties of BeO in its ambient and high-pressure phases *J. Phys. Chem. Solids* **70** 789–795

[9] Xu Y N and Ching W Y 1993 Electronic, optical, and structural properties of some wurtzite crystals *Phys. Rev. B* **48**(7) 4335–4351

[10] Marnetto A, Penna M, Bertazzi F, Bellotti E and Goano M 2009 *Ab initio*, nonlocal pseudopotential, and full-zone $k \cdot p$ computation of the electronic structure of wurtzite BeO *Opt. Quantum Electron.* **40**(14) 1135–1141

[11] Ahn D, Park S H, Park E H and Yoo T K 2006 Optical gain and luminescence of a ZnO-MgZnO quantum well *IEEE Photon. Technol. Lett.* **18**(2) 349–351

[12] Noel Y, Zicovich-Wilson C M, Civalleri B, D'Arco P and Dovesi R 2001 Polarization properties of ZnO and BeO: An *ab initio* study through the Berry phase and Wannier functions approaches *Phys. Rev. B* **65**(1) 014111

[13] Li S, Li Z Q, Shmatov O, Xia C S and Lu W 2005 3D simulations on realistic GaN-based light-emitting diodes in *2005 MRS Fall Meeting* (MRS) vol 892, Materials Research Society Symposium Proceedings pp 0892–FF12–12

[14] Chiaria S, Goano M and Bellotti E 2011 Numerical study of ZnO-based LEDs *IEEE J. Quantum Electron.* **47**(5) 661–671

[15] Dietl T, Ohno H and Matsukura F 2001 Hole-mediated ferromagnetism in tetrahedrally coordinated semiconductors *Phys. Rev. B* **63** 195205

[16] Vogel D, Krüger P and Pollmann J 1996 Self-interaction and relaxation-corrected pseudopotentials for II-VI semiconductors *Phys. Rev. B* **54**(8) 5495–5511

[17] Suzuki M, Uenoyama T and Yanase A 1995 First-principles calculations of effective-mass parameters of AlN and GaN *Phys. Rev. B* **52**(11) 8132–8139

[18] Kim K, Lambrecht W R L, Segall B and van Schilfgaarde M 1997 Effective masses and valence-band splittings in GaN and AlN *Phys. Rev. B* **56**(12) 7363–7375

[19] Goano M, Bertazzi F, Penna M and Bellotti E 2007 Electronic structure of wurtzite ZnO: Nonlocal pseudopotential and *ab initio* calculations *J. Appl. Phys.* **102**(8) 083709

[20] Dong L and Alpay S P 2011 Theoretical analysis of the crystal structure, band-gap energy, polarization, and piezoelectric properties of ZnO-BeO solid solutions *Phys. Rev. B* **84** 035315

[21] Dong L and Alpay S P 2012 Role of heteroepitaxial misfit strains on the band offsets of $Zn_{1-x}Be_xO$/ZnO quantum wells: A first-principles analysis *J. Appl. Phys.* **111**(11) 113714

[22] Ambacher O, Foutz B, Smart J, Shealy J R, Weimann N G, Chu K, Murphy M, Sierakowski A J, Schaff W J, Eastman L F, Dimitrov R, Mitchell A and Stutzmann M 2000 Two dimensional electron gases induced by spontaneous and piezoelectric polarization in undoped and doped AlGaN/GaN heterostructures *J. Appl. Phys.* **87**(1) 334–344

[23] Arora N D, Hauser J R and Roulston D J 1982 Electron and hole mobilities in silicon as a function of concentration and temperature *IEEE Trans. Electron Devices* **29**(2) 292–295

[24] Masetti G, Severi M and Solmi S 1983 Modeling of carrier mobility against carrier concentration in arsenic-, phosphorus-, and boron-doped silicon *IEEE Trans. Electron Devices* **30**(7) 764–769

[25] Furno E, Chiaria S, Penna M, Bellotti E and Goano M 2010 Electronic and optical properties of $ZnO/Mg_xZn_{1-x}O$ and $ZnO/Be_xZn_{1-x}O$ quantum wells *J. Electron. Mater.* **39**(7) 936–944

[26] Furno E, Bertazzi F, Goano M, Ghione G and Bellotti E 2008 Hydrodynamic transport parameters of wurtzite ZnO from analytic- and full-band Monte Carlo simulation *Solid-State Electron.* **52**(11) 1796–1801

[27] Heinemann M and Heiliger C 2011 Auger recombination rates in znmgo from first principles *J. Appl. Phys.* **110**(8) 083103 (pages 4) URL `http://link.aip.org/link/?JAP/110/083103/1`

[28] Chiaria S, Furno E, Goano M and Bellotti E 2010 Design criteria for near-ultraviolet GaN-based light-emitting diodes *IEEE Trans. Electron Devices* **57**(1) 60–70

[29] Mymrin V F, Bulashevich K A, Podolskaya N I, Zhmakin I A, Karpov S Y and Makarov Y N 2005 Modelling study of MQW LED operation *Phys. Stat. Sol. (c)* **2**(7) 2928–2931

[30] Sabathil M, Laubsch A and Linder N 2007 Self-consistent modeling of resonant PL in InGaN SQW LED structure in *Light-Emitting Diodes: Research, Manufacturing, and Applications XI (San Jose, CA, 2007)* vol 6486, Proceedings of the SPIE

[31] Xie J, Ni X, Fan Q, Shimada R, Özgür Ü and Morkoç H 2008 On the efficiency droop in InGaN multiple quantum well blue light emitting diodes and its reduction with *p*-doped quantum well barriers *Appl. Phys. Lett.* **93** 121107

[32] Chen T M, Wang S J, Uang K M, Kuo H Y, Tsai C C, Lee W C and Kuan H 2008 Current spreading and blocking designs for improving light output power from the vertical-structured GaN-based light-emitting diodes *IEEE Photon. Technol. Lett.* **20**(9) 703–705

[33] Li C K and Wu Y R 2012 Study on the current spreading effect and light extraction enhancement of vertical GaN/InGaN LEDs *IEEE Trans. Electron Devices* **59**(2) 400–407